J. Hydrol. Hydromech., 74, 2026, 1, 57–73
https://doi.org/10.2478/johh-2026-0005

Journal of Hydrology and Hydromechanics

Numerical study of transient flow dynamics in a prismatic channel with a bed depression

Shahin Oodi[1], Alireza Khoshkonesh[2], Saeid Okhravi[3*], Saeed Gohari[1*]

[1] Water Science Engineering Department, Faculty of Agriculture, Bu-Ali Sina University, Hamedan 65175-4161, Iran.
[2] Department of Geography, Birkbeck University of London, London WC1E 7HX, UK.
[3] Institute of Hydrology, Slovak Academy of Sciences, Dúbravská cesta 9, 84104, Bratislava, Slovakia.
[*] Corresponding author. E-mail: s.gohari@basu.ac.ir and saeid.okhravi@savba.sk

Abstract: Catastrophic floods triggered by a dam-break pose significant hazards to infrastructure due to transient flows and concentrated structural loads. These hazards are intensified where in-channel structures or variable topography redirect momentum and magnify impacts on downstream infrastructures. This study aimed to numerically predict the dam-break transient flow characteristics around a bed depression, as a specific topographic condition, in the downstream channel. The numerical model was optimized and validated against experimental results reported in the literature. Subsequently, the effects of bed depression dimensions and location along the channel on transient flow were examined in twelve cases. The validation results demonstrated that the model accurately reproduced the evolution of the free surface, flow velocity, formation of the impact jet, and impact loads. The bed depression has increased plunge-pool dissipation and reduced the peak force to 16.6–18.6 N. Accordingly, the supercritical flow was characterized by a maximum Froude number (Fr) of approximately 5.4 around this depression. Increasing the depression distance attenuated the wave front and decreased the post-depression flow depth from 0.16 m to 0.03 m within approximately 2 seconds. Overall, the framework captured sharp interfaces and transient regime shifts, enabling the prediction of jetting, nappe stabilization and impact-load envelopes. The study has implications for evaluating in-channel structures and the effects of channel topography on rapid flood hazard screening and emergency planning.

Keywords: Transient flow dynamics; Bed depression; Volume of Fluid (VOF); Numerical modeling; Impact loads.

1 INTRODUCTION

Dam failures are a global concern, generating rapidly evolving floods that impose severe, localized loads on infrastructure and downstream communities worldwide (Deng et al., 2018; Harrison et al., 2018). During such transient events, complex channel topography and in-channel structures can strongly redirect momentum, intensify turbulence, and concentrate impact forces (Liu et al., 2025; Meng et al., 2022). Among these features, bed depressions constitute common engineered or natural singularities that exert disproportionate control over nappe development, hydraulic-jump behavior, and energy dissipation (Fan et al., 2021; Mahmoud and Uchida, 2024). Accurate prediction of these processes, therefore, requires high-fidelity free-surface modeling capable of resolving sharp interfaces, rapid regime transitions, and strong flow–bed interactions, supported by robust validation (Zhu and Hu, 2018). In this context, although dam failures are a primary motivation for the present work, similar surge waves in open channels may also arise from other transient mechanisms, such as rapid gate operations, sudden releases, or large mass movements. Accordingly, this study addresses the hydraulic response to a generalized transient surge, with dam-break flow serving as a representative and well-defined forcing scenario. At the same time, recent climatic intensification and ongoing urban expansion have substantially increased exposure to such extreme events, thereby amplifying the demand for dependable, physics-based guidance for emergency planning and mitigation (Ma et al., 2025; Maranzoni et al., 2024). However, despite this growing practical urgency, many existing studies still overlook the influence of discrete bed depressions on jet formation and the associated transient restructuring of the flow field (Zhou et al., 2022).

A substantial body of research has advanced the understanding of transient flow hydraulics through analytical, numerical, and experimental approaches. In particular, Ni et al. (2019) and Wang et al. (2020) extended classical shallow-water formulations to describe wave-tip propagation and bore evolution in wet-bed channels. However, such depth-averaged models typically neglect local three-dimensional vortices and vertical accelerations near bed discontinuities. This limitation restricts their applicability to flows governed by abrupt geometric features. Addressing localized flow complexity, Velísková et al. (2018) combined laboratory ADV measurements with RANS-based simulations to investigate flow behind overflooded obstacles. Their results revealed pronounced velocity-profile deformation and persistent wake complexity downstream. Their analysis demonstrated that CFD models can reliably capture near-wake flow features. It also identified the downstream extent over which predictions remain physically consistent. Similarly, Říha et al. (2019) evaluated shallow-water model performance for flow over trapezoidal broad-crested weirs. Their study accounted for vertical flow contraction and systematically varied surface roughness under frontal overflow conditions. The resulting discharge-coefficient deviations of approximately 2–10% clearly delineated the practical limits of depth-averaged formulations near abrupt topographic transitions. Extensions of reduced-order models have also been proposed. Cozzolino et al. (2018) incorporated porosity effects and developed exact Riemann solutions that provide valuable

benchmarks for model validation near discontinuities. However, their direct application to irregular or non-prismatic channels remains constrained. Moving beyond hydrostatic assumptions, Zhu and Hu (2018) introduced vertical non-hydrostatic solvers and variational frameworks for dispersive and submerged jumps. These approaches enabled a more realistic representation of rapidly varied free-surface flows. In parallel, high-fidelity numerical simulations have expanded insight into transient flow behavior. Meng et al. (2022) resolved mobile-bed interactions and three-dimensional jet impacts near hydraulic structures. Their work also captured sediment-laden dam-break fronts with high spatial resolution. Mattas et al. (2023) demonstrated that two- and three-dimensional CFD models more accurately reproduce jet dynamics and tailwater effects. Complementary validations by Hien and Van Chien (2021) confirmed reliable prediction of pressure peaks on downstream building arrays under high-Froude conditions. Experimental investigations remain indispensable, as shown by Aureli et al. (2023) and Maranzoni et al. (2024). These studies quantified the influence of mobile beds using synchronized free-surface, velocity, and pressure measurements. Beyond hydrodynamic modeling, Abdedou et al. (2020) introduced non-intrusive uncertainty quantification linking dynamic waves to societal risk. Fan et al. (2021) demonstrated that groynes and downstream lakes can substantially attenuate bore height and celerity. At a broader spatial scale, Harrison et al. (2018) documented geomorphic pulses following dam removal and cascading check-dam failures. Pandey et al. (2024) and Xu et al. (2025) showed the superiority of dynamic-wave approaches over diffusion-wave models in complex terrain. Collectively, these studies indicate substantial progress. However, systematic parametric understanding of three-dimensional transient flow over bed depressions remains limited, particularly regarding energy dissipation and structural loading.

This literature synthesis shows that, despite significant advances, critical knowledge gaps persist for bed depressions under dam-break forcing and high-Froude transient flows. Table 1 synthesizes representative studies by flow regime, geometry, methodology, principal findings, and limitations, clarifying how existing work addresses isolated aspects of the problem. Accordingly, most studies consider simplified obstacles or single configurations, while systematic three-dimensional parametric analyses remain scarce (Dezert et al., 2024; Rajaie et al., 2022). Such investigations are rarely supported by coordinated experimental validation, limiting confidence in predicted three-dimensional vortices, vertical accelerations, and secondary currents near depressions.

Table 1. Representative studies of transient flows over bed irregularities summarizing methods, geometries, findings and limitations.

Study by.	Geometry considered	Method	Key findings	Main limitation
Deng et al. (2018)	Flat bed	Analytical / SWE	Described wave-tip propagation and bore evolution	Neglects 3D effects and vertical accelerations
Ni et al. (2019)	Steep slope, smooth bed	Extended SWE	Improved prediction of bore propagation	Inapplicable near abrupt bed discontinuities
Wang et al. (2020)	Triangular channel	SWE + experiments	Captured wave propagation and front evolution	Depth-averaged formulation
Velísková et al. (2018)	Overflooded obstacle	RANS + ADV	Identified wake complexity and velocity deformation	Single obstacle geometry
Říha et al. (2019)	Trapezoidal weir	SWE + experiments	Quantified discharge-coefficient deviations	Limited to frontal overflow
Cozzolino et al. (2018)	Porous discontinuity	SWE with Riemann solutions	Provided exact benchmarks near discontinuities	Limited applicability to irregular channels
Zhu and Hu (2018)	Idealized bed	Non-hydrostatic SWE	Captured vertical accelerations and dispersive jumps	Reduced dimensionality
Meng et al. (2022)	Local structure	3D CFD	Captured jet impact and sediment interaction	Case-specific configuration
Hien and Van Chien (2021)	Building arrays	2D/3D CFD	Predicted pressure peaks on structures	Simplified upstream geometry
Aureli et al. (2015)	Vertical wall	Experiments + CFD	Quantified impact forces and pressure peaks	No bed irregularities
Aureli et al. (2023)	Fixed bed	Experimental review	Synthesized pressure and velocity measurements	Fragmented geometry coverage
Fan et al. (2021)	Lake / groyne system	Experiments + modeling	Demonstrated wave attenuation mechanisms	Not focused on bed depressions
Abdedou et al. (2020)	Idealized reach	Stochastic modeling	Linked hydraulic uncertainty to risk metrics	No local flow-structure resolution
Rajaie et al. (2022)	Flat bed, structure	Experiments	Measured impact loads under high-Froude flow	No bed depressions
Dezert et al. (2024)	Rockfill dam models	Experiments	Evaluated parametric breach effects	Focus on breach, not downstream bed
Oguzhan and Aksoy (2020)	Vegetated bed	Experiments	Identified vegetation effects on bore attenuation	No impact-load characterization

Table 1 further indicates that concurrent characterization of jet evolution and time-resolved impact loads is uncommon (Aureli et al., 2023; Hien and Van Chien, 2021; Oguzhan and Aksoy, 2020). Consequently, linkages between transient jet dynamics, peak structural loading, and energy-dissipation pathways remain insufficiently resolved across existing studies. Moreover, translation of these hydraulic processes into risk-screening tools and dissipator design guidance remains fragmented across hydraulic, structural, and risk-analysis disciplines (Abdedou et al., 2020; Fan et al., 2021; Khoshkonesh et al., 2024). To address these gaps, the present study adopts a unified flow–structure interaction framework using a validated three-dimensional Navier-Stokes Volume-of-Fluid solver. The model is calibrated against multiple laboratory datasets and applied to twelve configurations spanning depression geometry and downstream position. This approach enables systematic assessment of front steepening, jet formation, nappe stabilization, Froude-number evolution, and energy-dissipation mechanisms across representative conditions.

Despite extensive research on dam-break flows, Table 1 shows that the hydraulic role of bed depressions remains insufficiently resolved. Most previous studies rely on depth-averaged models, idealized geometries, or isolated obstacles, limiting their ability to capture three-dimensional transient flow restructuring. In particular, the combined effects of depression geometry and streamwise position on wave-front evolution, jet formation, and impact loading are largely unexplored. Existing three-dimensional studies typically examine single configurations, preventing systematic isolation of geometric influences under high-Froude conditions. To address these gaps, the present study investigates transient dam-break flow over a bed depression in prismatic channels using a validated three-dimensional CFD framework. The novelty lies not in the numerical solver, but in its systematic, physically integrated application to an unresolved hydraulic problem. A controlled parametric analysis varies depression depth, length, width, and position across twelve configurations to isolate their individual and combined effects. The jet development, nappe stability, and time-resolved impact loads are analyzed concurrently, linking transient flow restructuring to structural loading mechanisms. These dynamics are translated into interpretable metrics relevant to risk screening and energy-dissipation design, including Froude-number fields and peak-load reduction. Together, the results provide geometry-resolved insight that complements existing studies and supports improved assessment of dam-break hazards.

2 METHODOLOGY

In this study, the transient flow dynamics were estimated by assuming an incompressible, viscous flow, in which the fluid fraction V_f is used to activate the Navier-Stokes equations only within the occupied portion of each control volume. The mass conservation and momentum transport are therefore written in the following form (Eqs. 1 and 2) (Heidarian et al., 2025):

$$\frac{\partial}{\partial t}\left(\rho V_f\right) + \nabla\left(\rho V_f u\right) = 0 \tag{1}$$

$$\frac{\partial}{\partial t}\left(\rho V_f u\right) + \nabla\left(\rho V_f uu\right) = -V_f \nabla_p + \nabla[\mu(\nabla u + \nabla u^T)] + \rho V_f g \tag{2}$$

where g is the body force due to gravity, and μ, ρ, and v represent the dynamic viscosity, fluid density, and kinematic viscosity, respectively, and V_f represents the volume of fluid. The volume fraction V_f scales the advective and source terms so that momentum is updated within the fluid-occupied portion of each cell. Momentum evolution is controlled by pressure gradients, viscous stresses, gravity, and advection, with air entrainment indirectly modifying these processes through its effect on the mixture density and viscosity (Khoshkonesh et al., 2019).

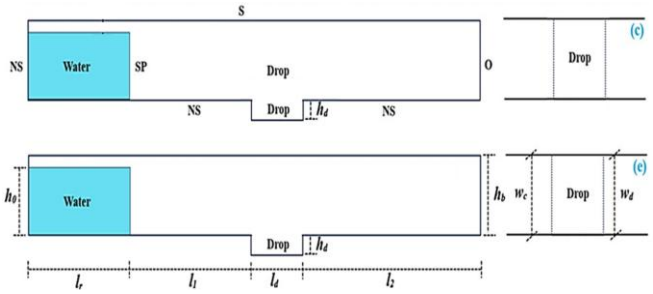

Fig. 1. Schematic configuration of the transient dam-break flow over the bottom depression models, with initial and boundary conditions.

The volume-of-fluid function F is simultaneously advanced through an advection equation (Eq. (3)):

$$\frac{\partial F}{\partial t} + u\,(\nabla F) = 0 \tag{3}$$

Each control volume stores a volume fraction, $0 \le F \le 1$, which defines the position of the free surface. This coupling between V_f in the momentum equation and F in the interface advection enables FLOW-3D (Version V.12; https://flow3d.com; Flow Science, Inc.) to conserve both mass and momentum while accurately capturing the moving air-water boundary (Hirt and Nichols, 1981).

In addition to the standard volume-of-fluid formulation, an air-entrainment model was activated to account for the entrainment and transport of dispersed air in highly aerated regions of the transient flow (Hirt and Nichols, 1981). The local air volume fraction α is governed by a scalar transport equation (Eq. (4)).

$$\frac{\partial \alpha}{\partial t} + \nabla(\alpha u) = S_e - S_d \tag{4}$$

where S_e and S_d represent air entrainment and detrainment source terms, respectively. The entrainment source term is activated when local turbulent kinetic energy and free-surface curvature exceed threshold values, consistent with jet impact and surface breakup. The resulting mixture density and viscosity are computed as Eqs. (5) and (6).

$$\rho_m = \alpha\rho_a + (1-\alpha)\rho_w \tag{5}$$

$$\mu_m = \alpha\mu_a + (1-\alpha)\mu_w \tag{6}$$

where subscripts a and w denote air and water phases. These mixture properties are used in the momentum equations, allowing aeration to influence predicted flow depths, pressures and impact forces. This formulation improves the representation of jet cushioning and pressure attenuation effects while maintaining numerical stability in strongly transient free-surface regions.

Air entrainment and entrapment remain challenging to represent accurately, as both laboratory experiments and numerical simulations are limited in resolving fully aerated,

highly transient free-surface flows. Accordingly, aeration is included to capture its first-order influence on mixture properties and impact force attenuation, rather than to claim complete physical fidelity of aeration processes. This formulation is intended to represent the dominant cushioning effect of air on pressures and loads, while acknowledging unresolved small-scale aeration dynamics.

2.1 Turbulence modeling

To represent turbulent motion, various closure strategies can be employed, depending on the desired level of resolution. Reynolds-Averaged Navier-Stokes (RANS) models replace the instantaneous velocity field with a mean component $\bar{u}$, and turbulent fluctuations u', and solve the ensemble-averaged momentum equations. This approach accounts for the net effect of turbulent eddies on the mean flow but does not explicitly resolve their instantaneous dynamics (Okhravi et al., 2023). In contrast, the Large Eddy Simulation (LES) technique directly computes the dynamics of the energy-containing, larger turbulent structures. It introduces a sub-grid scale (SGS) stress tensor to represent motions smaller than the grid filter width Δ. The spatially filtered momentum equation used in LES can be written as follows (Eq. 2 is rewritten as Eq. 7) (Heidarian et al., 2025; Oyem et al., 2025).

$$\frac{\partial}{\partial t}(\rho\tilde{u}) + \nabla\left(\rho V_f \tilde{u}\tilde{u}\right) = -V_f\nabla_p + \nabla\left[(\mu + \mu_{SGS})(\nabla\tilde{u} + \nabla\tilde{u}^T)\right] + \rho V_f g \quad (7)$$

where $\tilde{u}$ and $\tilde{p}$ represent the filtered velocity and pressure fields, and μ_{SGS} is the eddy viscosity supplied by the chosen SGS model (e.g., Smagorinsky). LES typically yields higher-fidelity predictions of transient vortical structures and free-surface deformation than RANS, albeit at a greater computational cost (Khoshkonesh et al., 2024; Maskoni et al., 2023). For numerical stability, the Courant-Friedrichs-Lewy (CFL) condition is enforced so that $u\Delta t/\Delta x \leq 1$. Simulations were iterated until the global residuals of all solved quantities stepped below 10^{-3}, which was adopted as the convergence criterion (Hui et al., 2024).

2.2 Initial and boundary conditions

The initial conditions (ICs) were prescribed by assigning the reservoir's stored water volume and its corresponding hydrostatic pressure distribution. In contrast, the specification of boundary conditions (BCs) played a more decisive role across the various regions of the computational domain (see Table 2). Throughout the formulation, the subscripts n and t denote components oriented normal and tangential to the respective boundary surfaces. As shown in Fig. 1, the investigated configuration consists of a local transverse depression formed by a negative bottom step followed by a positive step. The downstream positive step is introduced solely to restore the original bed elevation and ensure a localized geometric perturbation. The hydraulic response analyzed in this study is governed primarily by the negative step, which controls flow separation, jet formation, and impact processes. Accordingly, the term "bed depression" is used throughout the paper to describe this configuration.

2.3 Error formulation

The model reliability and predictability were evaluated using root mean square error (RMSE), mean absolute error (MAE), and coefficient of determination (R^2) (Eqs. 8 to 10).

$$RMSE = \sqrt{\frac{1}{n}\sum_{i=1}^{n}(X_e - X_i)^2} \quad (8)$$

$$MAE = \frac{1}{n}\sum_{i=1}^{n}|X_e - X_i| \quad (9)$$

$$R^2 < 1 - \frac{\sum_i (X_i - X_e)^2}{\sum_i (X_e - \overline{X_e})^2} \quad (10)$$

where n, X_i, X_e, and $\overline{X_e}$ represent the number of observations, the numerical and experimental values, and the mean value for the i-th observation, respectively.

2.4 Model calibration and validation

To ensure reliable numerical predictions, the modeling framework was systematically tuned and checked against benchmark experimental data reported in previous studies (Koshizuka and Oka (1996); Kleefsman et al. (2005); Ferrari et al. (2010); Kocaman and Ozmen-Cagatay (2012); Aureli et al. (2015)); Kocaman et al. (2021)). The refinement process followed two sequential tracks. First, a mesh-independence assessment was performed by running simulations with progressively smaller cell sizes until further grid refinement no longer produced meaningful changes in free-surface evolution or impact loads.

Second, a turbulence-model sensitivity study was conducted to compare RANS and LES closures. The approach that best reproduced the measurements was identified. Subsequently, the calibrated setup was rigorously validated by comparing predicted free-surface profiles, velocity fields and stage hydrographs with published laboratory observations. This validation against experimental data instills confidence in the model's reliability. This validated configuration was then used to examine how variations in bed geometry, orientation and distance from the dam influence wave propagation and impact characteristics (see Fig. 2).

Table 2. The initial and boundary conditions applied in the transient flow modeling.

Condition - Type	Acronym	Position	Formulation
No-slip (wall) - BC	NS	Bed and sidewalls	$\partial p/\partial x = 0, u = 0$
Specific pressure - BC	SP	Dam site	$p = \gamma h, \partial u/\partial x = 0$
Symmetry - BC	S	Upper boundaries	$\partial p/\partial n = 0, u_n = 0, \partial u_t/\partial n = 0$
Outflow - BC	O	Channel endpoint	$\partial p/\partial n = 0, \partial u/\partial n = 0, \partial v/\partial n = 0, \partial w/\partial n = 0$

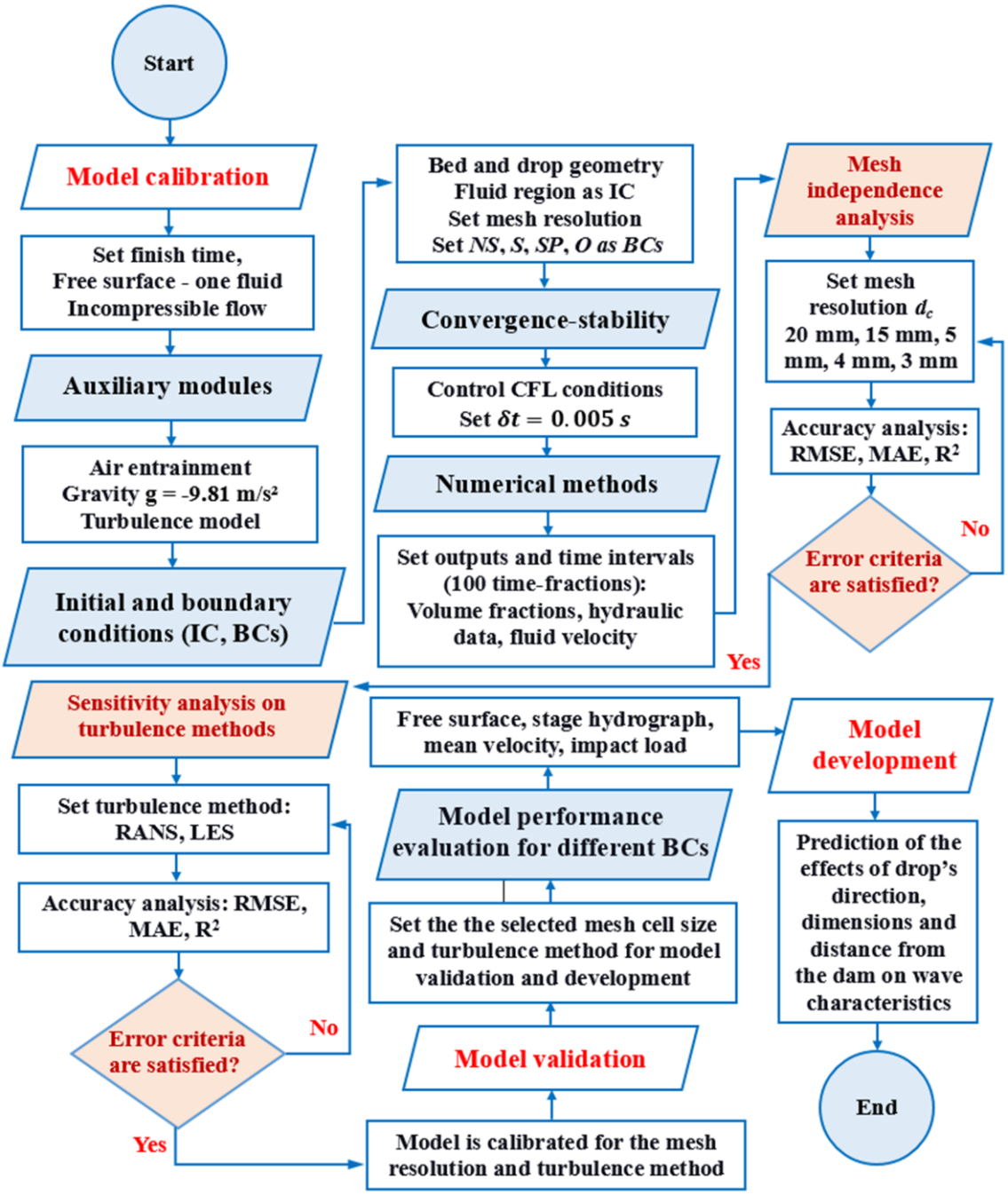

Fig. 2. Flowchart of the model optimization and the development in the 3D-VOF approach.

2.5 Scaling considerations and prototype extrapolation

The numerical simulations follow Froude similarity, which is appropriate for rapidly varying free-surface flows dominated by gravity and inertia (Heller, 2011). Under this framework, geometric lengths scale with λ, velocities scale with $\lambda^{1/2}$, time scales with $\lambda^{1/2}$, and hydrodynamic forces scale with λ^{3}. Accordingly, the present analysis emphasizes relative trends, spatial distributions and comparative reductions in force across bed-depression configurations, rather than the direct prediction of absolute prototype forces. This approach is consistent with established practice in laboratory and numerical studies of dam-break and spillway flows, where Reynolds numbers remain sufficiently high for viscous scale effects to be secondary (Catucci et al., 2021; Khoshkonesh et al., 2024). While extrapolation to prototype conditions must therefore be interpreted with caution, the adopted similarity framework provides physically meaningful guidance for hazard screening and dissipator design, particularly in terms of identifying geometries that mitigate peak impact loads and reorganize transient flow structures.

2.6 Model development for transient flow evolution over the bed depressions

The floods triggered by the failure of a dam have a profound impact on downstream areas, whether undeveloped or densely urbanized (Albu et al., 2020). The effects of natural or artificial singularities, such as river morphology, lakes, or infrastructures like bridges, ponds, or buildings, are only partially understood (Khoshkonesh et al., 2019).

Table 3. The experimental dam-break configurations used in the optimization of models.

Dam-break experiment	h_0, w_c, w_w, w_{op}, w_1, w_o, w_2, l_c, l_r, l_1, l_o, all dimensions in meters (m)	Optimization phase	Physical aspect
Kocaman et al. (2021)	0.15, 0.5, 0.2, 0.1, 0.18, 0.08, 0.18, 1, 0.25, 0.25, 0.15	Calibration	Free surface
Kocaman and Ozmen-Cagatay (2012)	0.25, 0.3, 0, 0.3, 0.1, 0.1, 0.1, 8.9, 4.65, 1.52, 0.95	Calibration	Free surface, outflow depth
Ferrari et al. (2010)	0.1, 2, 0.8, 0.4, 1, 0, 1, 3, 1, 0, 0	Calibration	Mean velocity
Kleefsman et al. (2005)	0.55, 1, 0, 1, 0.5, 0, 0.5, 3.22, 1.228, 0, 0	Validation	Jet formation
Koshizuka and Oka (1996)	0.292, 0.1, 0, 0.1, 0, 0.1, 0, 0.584, 0.146, 0.146, 0.024	Validation	Jet deformation
Aureli et al. (2015)	1.2, 0.45, 0.3, 0.45, 2.6, 0.8, 0.51, 0.155	Validation	Fluid force

This study models transient dam-break flows interacting with idealized bed depressions representing downstream structural components. Twelve numerical configurations were simulated to systematically examine the influence of bed-depression geometry and location on flow evolution. The computational domain, geometric configurations, and applied initial and boundary conditions for all cases are shown in Fig. 10. Identical initial conditions were imposed in all simulations, including a still-water reservoir depth of h_0 = 0.30 m and reservoir length l_r = 1.32 m. Depression orientation, depth, width, length, and stream wise position were treated as independent variables. Subsequently, the free-surface evolution, transient flow regime, jet development, and time-resolved impact loads were evaluated as dependent response variables.

3 RESULTS AND DISCUSSION

The model was optimized by fine-tuning critical parameters to improve accuracy and provide reliable predictions based on experimental results (see Table 2). The optimization process encompassed calibration and validation stages, each of which included a crucial aspect of model reliability. The physical elements predicted at each stage are presented in the last column of Table 3 and in Fig. 3. In Table 3 and Fig. 3, h_0 represents the initial water depth in the reservoir before breaking the dam (i.e., the static water column). The other parameters in Table 3 are depicted in Fig. 3. These dam-break (transient flow) experiments were selected because the wave-structure interactions were reported in all of them.

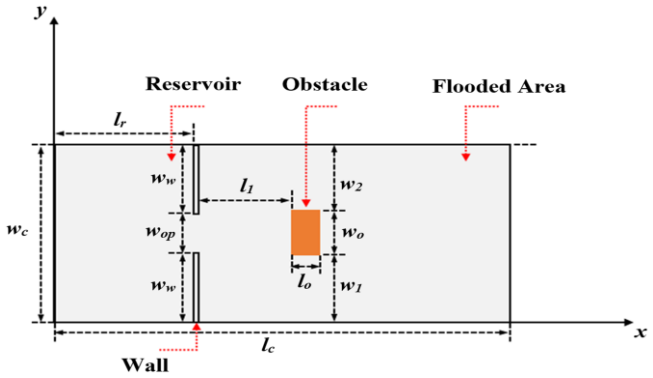

Fig. 3. Schematic unanimous configurations of dam-break experimental setups in mentioned studies, illustrating the reservoir, obstacles, downstream channel, and walls with their dimensions.

3.1 Numerical model calibration and sensitivity analysis

This section presents model calibration and numerical sensitivity analyses, whose sole purpose is to establish simulation reliability prior to addressing the study objectives. The calibration procedure was designed to constrain numerical and turbulence-model parameters governing free-surface deformation, momentum exchange and transient pressure loading, rather than to fit a specific bed geometry (Rahimpour et al., 2026). The laboratory data involving a positive step (baffle pier) were therefore employed, as they provide robust, well-resolved force measurements under rapidly varying, supercritical dam-break conditions. However, the laboratory measurements of dam-break flows over bed depressions are scarce in the literature. Although the sign of the bed discontinuity differs, both positive steps and bed depressions induce comparable flow regimes characterized by abrupt momentum changes, pressure redistribution and short-duration force peaks. The bed-depression cases examined in this study thus represent an independent evaluation of the calibrated model, allowing its predictive capability to be assessed for unreported geometries without further parameter adjustment. Therefore, a refinement study was conducted to confirm that the numerical solution was not sensitive to the mesh grid resolution. In this process, structured meshes with mean cell sizes of 20, 15, 10, 5, and 4 mm were generated while maintaining aspect ratios near unity (Figs. 4 and 5). The model's accuracy was evaluated by comparing the simulated free-surface stage hydrograph at a control section immediately downstream of the obstacle.

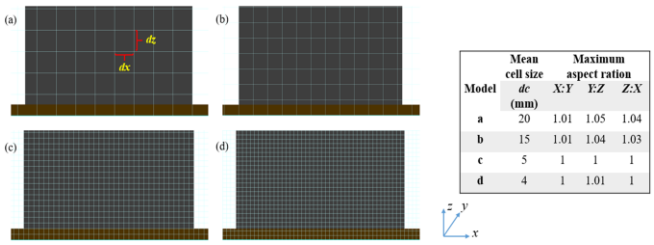

Model	Mean cell size dc (mm)	Maximum aspect ration X:Y	Y:Z	Z:X
a	20	1.01	1.05	1.04
b	15	1.01	1.04	1.03
c	5	1	1	1
d	4	1	1.01	1

Fig. 4. Mesh cells of different sizes covered the obstacle in the downstream channel.

For each mesh, total cell count, runtime, computational demand, and discretization error were carefully examined. As the grid was refined, the total element number rose sharply from about 2.0×10^5 cells at 20 mm to more than 3.7×10^6 cells at 4 mm (Fig. 5a). At the same time, runtime initially decreased from

roughly 10^3 s at 20 mm to about 10^2 s at 15 mm due to improved solver stability; however, it then increased steeply beyond 10^4 s for the finest meshes (Fig. 5b). The smallest grid consequently required approximately nine hours of computation on an Intel® Core™ i7-1165G7 (11th Gen, eight threads, 16 GB RAM).

Moreover, discretization uncertainty stepped markedly as the grid was refined. It decreased from nearly 100% at 20 mm to below 10% when the spacing reached 5 mm, and it remained low at 4 mm (Fig. 5c). This trend indicated that further refinement beyond 4 mm would add considerable cost without yielding meaningful accuracy gains. Correlation analysis also revealed a powerful relationship between total cells and run time ($R \approx 0.95$) and a moderate link between cycle count and elapsed simulation time (Fig. 5d).

Considering these results, the grid with a 4 mm mean cell size was ultimately selected. This configuration provided stable free-surface predictions, met mesh quality thresholds, and minimized discretization error. It also achieved an acceptable compromise between computational effort and numerical accuracy.

A targeted sensitivity study was performed to evaluate turbulence models and align the simulations with established laboratory measurements. Specifically, the experimental datasets from Kocaman and Ozmen-Cagatay (2012) and Ferrari et al. (2010) were selected because they report detailed free-surface elevations, outflow depths, and depth-averaged velocities under dam-break conditions. Consequently, both RANS and LES models were assessed to identify the most reliable option. The model accuracy was first examined for free-surface elevation. In this case, the LES approach reproduced the observed water surface with high agreement, yielding $R^2 = 0.9213$, RMSE = 0.013 m, and MAE = 0.009 m, while RANS produced similar but slightly lower fidelity (Figs. 6a,b).

Subsequently, the reservoir outflow depth predictions were then compared. Here, both the RANS and LES models closely matched the measurements, achieving R^2 values of 0.9976 and 0.9978, respectively, with RMSE values of 0.007 m and 0.006 m (Figs. 6c,d). These results indicate that either turbulence treatment can reproduce discharge depths with minimal error. Next, the depth-averaged velocity evaluation highlighted more apparent differences. Notably, the LES model also achieved an R^2 of 0.9123, an RMSE of 0.065 m/s, and an MAE of 0.009 m/s, while RANS showed slightly higher scatter and a larger mean error (Figs. 6e,f). This suggested that the RANS solution tended to overestimate peak flow speeds, likely due to under-representation of local resistance and small-scale energy losses. Overall, the LES method consistently reproduced free-surface heights and mean velocity fields more accurately than RANS, while maintaining comparable accuracy in the outflow depth. Therefore, LES was selected for subsequent model optimization and final simulation stages. It improved predictive reliability without introducing additional numerical instability.

All subsequent sections present results obtained using the calibrated configuration and focus exclusively on addressing the study objectives related to bed-depression effects.

3.2 Model validation against the experimental results of the previous studies

The transient flow evolution downstream of the channel and its impact on the obstacle may lead to a jet-like flow above it. The jet-like flow deformation, its sleeping over the downstream channel, and its impact load are critical phenomena in numerical simulations. The model was validated against numerous experimental results (Figs. 7 and 8). As shown in Fig. 7a, the model had high accuracy in reproducing the free surface curvature within the reservoir, W-R1 (wave region 1). Accordingly, the model efficiently predicted the steeped slope region of W-R2. Impacting the wavefront, W-R3, on the obstacle led to the formation of an upward jet-like flow, J-R1 (jet region 1), flow separation, and passing the wave by the side of the depression in Fig. 7b. Overall, the model showed high performance in reproducing the wave evolution and jet-like flow development.

The model's validation against the experimental results of Koshizuka and Oka (1996) showed that the model had high accuracy in predicting the upward jet-like flow deformations after impact on the downstream obstacle (Figs. 8a,b). An inflection point was observed in the tongue-like jet flow in both experimental and numerical results (between JR-1 and JR-2). The length of the jet at region JR-2 was about higher in the numerical results (Fig. 8c). Then, the tongue-like jet impacted the downstream wall in both experimental and numerical results (JR-3), as shown in Fig. 8d. Finally, the model performance in predicting the horizontal force (impact load) exerted by the wave on the obstacle was evaluated using the experimental results of Aureli et al. (2015), as can be seen in Fig. 9. The model performance in predicting the impact load was acceptable; however, the model overestimated the peak impact load by approximately the peak impact load by approximately F_x = 4–6 N.

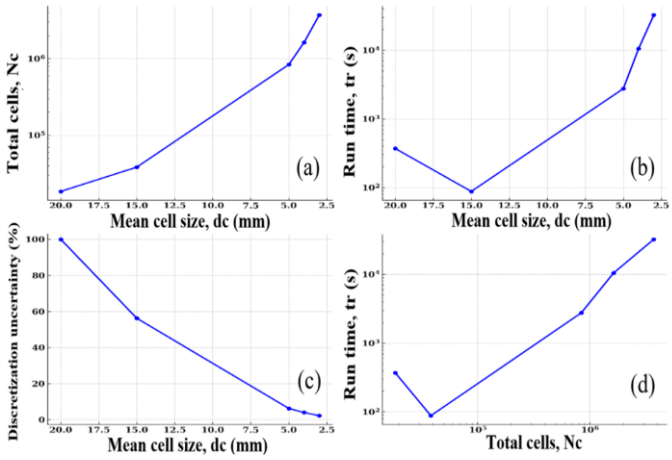

Fig. 5. Mesh resolution and computational cost analysis with estimated discretization uncertainty for the CFD simulations.

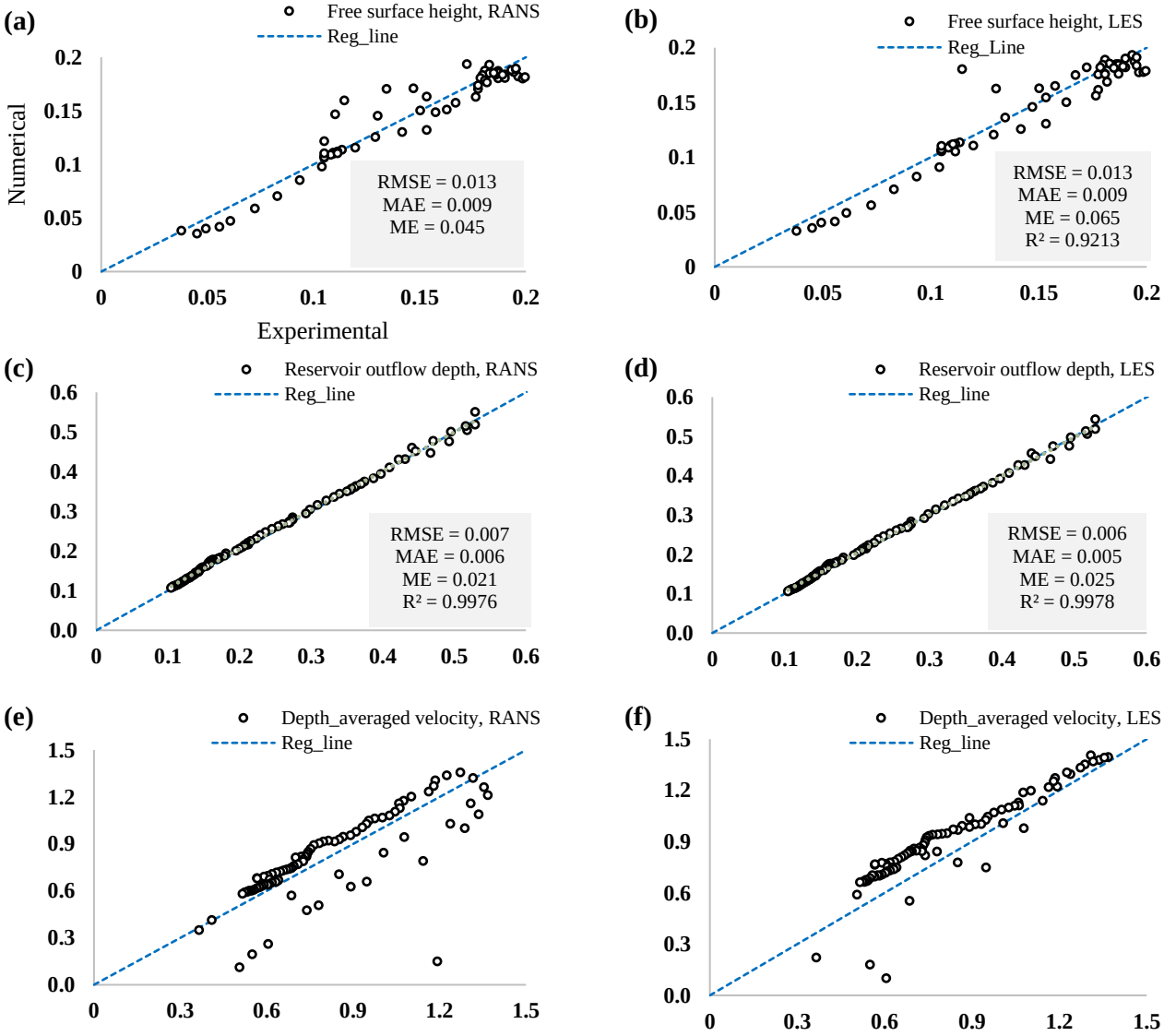

Fig. 6. Comparative analysis of model calibrations for the (a) and (b) free surface height, (c) and (d) reservoir outflow depth, and (e) and (f) depth-averaged velocity in RANS and LES, respectively (Exp: (a) to (d) Kocaman and Ozmen-Cagatay, 2012; (e) and (f) Ferrari et al., 2010).

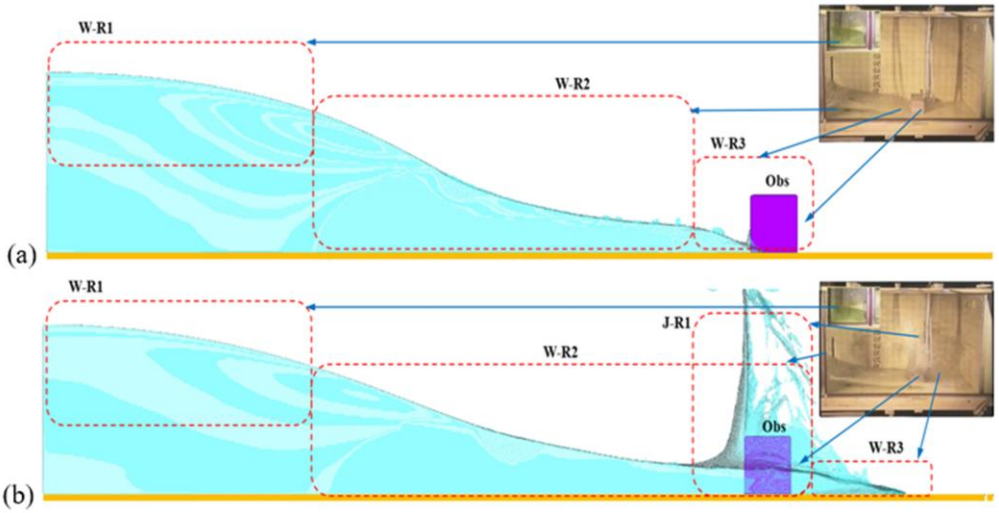

Fig. 7. Model performance in prediction of (a) and (b) wave evolution and jet-like flow formation validated with experimental results of Kleefsman et al. (2005).

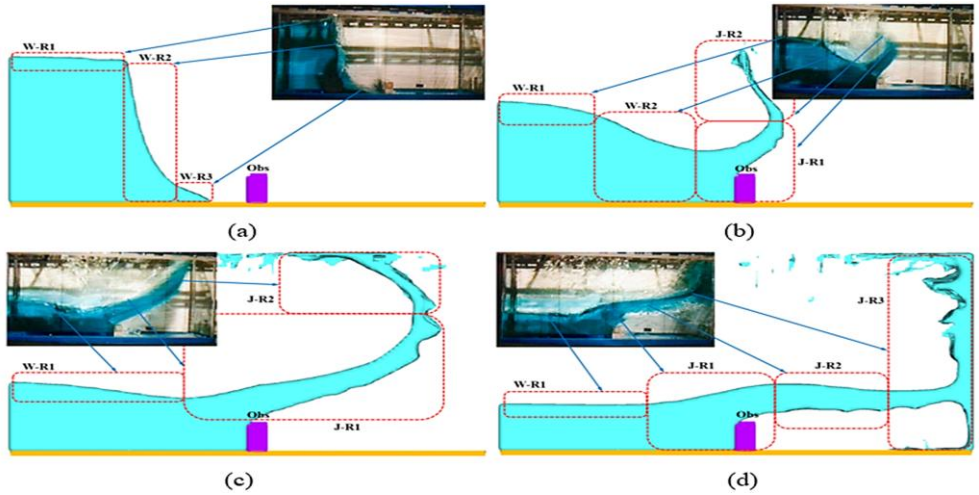

Fig. 8. Dam-break wave evolution and jet-like flow deformation in (a) t = 0.1 s, (b) t = 0.2 s, (c) t = 0.3 s, and (d) t = 0.4 s, validated with experimental results of Koshizuka and Oka (1996).

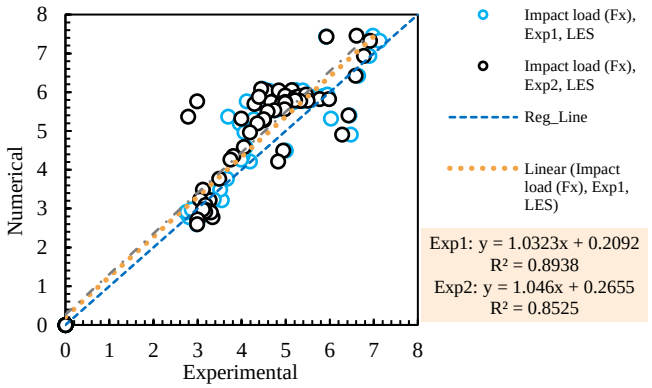

Fig. 9. Dam-break impact load in the horizontal direction, validation with experimental results of Aureli et al. (2015).

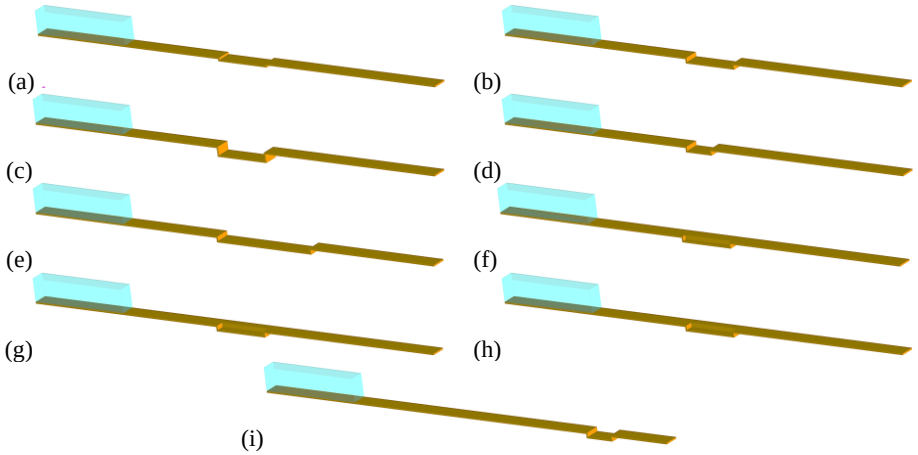

Fig 10. Configuration of the transient flow over the channel with a bottom depression models for the different (a) to (c) step's depth, (d) and (e) step lengths, (f) and (g) step widths, and (h) and (i) step location along the channel.

3.3 Transient flow evolution analysis

The physical aspects of wave evolution over the channel with singularities were simulated during δt = 2 *s* of the phenomenon based on the computational domain illustrated in Fig. 10, exhibiting significant variation in dynamic characteristics. For the bed depression, increasing the height, from 27.5 mm to 110 mm, resulted in a deeper plunge pool, which could absorb more of the nappe flow energy. As the bed depression became deeper, the free surface showed a thicker, more aerated nappe with stronger surface breakup, indicating higher local energy dissipation. It reduced the initial wave impact but potentially caused a more turbulent hydraulic jump.

The deeper bed depression also altered the downstream flow regime, with implications for channel stability. In addition, an apparent delay and flattening of the advancing wavefront appeared as bed-depression height increased, showing reduced celerity and enhanced flow attenuation. Increasing the bed-depression height also reduced the horizontal extent of the wavefront travel distance and wave celerity due to increased energy losses and changes in wave energy (Fig. 11). It is worth noting that Fig, 11g depicts a distinctive flow regime in which the nappe, plunging over the deep bed depression, generates a

pronounced vertical jet that reaches an elevation exceeding the initial reservoir head. This phenomenon results from the highly transient, impulsive nature of the dam-break flow interacting with a nearby bed depression. The initial bore possesses significant kinetic energy, which, upon impact with the lower bed, is not merely dissipated but partially redirected. This localized momentum transfer can generate a coherent, upward-moving water mass, a dynamic jetting effect. The energy for this jet originates from the concentrated kinetic energy of the impacting bore, not solely from the initial static head. Furthermore, the simulation of the free surface after the nappe impact, particularly the generation of spray and droplets (e.g., Fig. 11g), should be interpreted with caution. While the VOF method and air entrainment module capture the bulk air-water interface dynamics well, the fragmentation into fine droplets and the trajectory of splashed water are influenced by sub-grid-scale processes and interfacial tension models. The predicted elevation of the spray may therefore represent the resolved scale of the aerated, turbulent mixture rather than the precise trajectory of individual water particles. Future work employing coupled VOF-DPM (Discrete Phase Model) methods could better quantify this aspect.

The transient flow evolution over the channel with varying bed depression lengths was simulated for 2 s, revealing distinct flow responses. Increasing the bed-depression length, from 345 mm to 1380 mm, produced an extended falling water sheet that traveled farther before contacting the lower bed. With longer bed depression, the downstream water surface appeared flatter and more uniform after impact, suggesting a gentler transition to subcritical flow. This geometry reduced abrupt plunging and promoted a smoother adjustment of the free surface beyond the bed depression. The altered length also displaced the hydraulic transition farther downstream, modifying where energy dissipation concentrated and where sediment transport might initiate. Moreover, longer depressions visibly delayed the arrival of the leading wave and broadened the flow front, indicating greater attenuation and slower overall propagation. Collectively, the wave-front morphology and the hydraulic adjustment zone were firmly controlled by the bed-depression length. Extending the depression increased the reach of the nappe, redistributed energy losses over a longer distance, and reduced the effective forward advance of the wavefront due to enhanced dissipation (Fig. 12). In the limiting case of a very narrow bed-depression or transverse depression, lateral spreading of the nappe is strongly constrained. As a result, the dam-break wave predominantly skims or shoots over the unevenness, with only a minor adjustment in flow depth. In this regime, consistent with the narrow-width cases examined in this study, the depression behaves as a weak geometric perturbation rather than a controlling hydraulic element, and the flow remains strongly supercritical over a short adjustment length. Enlarging the depression width, from 50.5 mm to 202 mm, created a broader nappe that spread laterally before reattaching to the downstream channel. With wider depression, the water surface immediately downstream became thinner and stretched sideways, reducing the local flow depth directly under the falling jet.

This configuration lessened concentrated impact but distributed the inflow momentum across a larger section of the bed. The altered width also shifted the hydraulic jump formation, which appeared more diffuse and migrated slightly downstream as the depression widened. Furthermore, greater width slowed the advancing wave front and promoted a wider, less steep leading edge, indicating additional energy dispersion. Altogether, the wave evolution and hydraulic adjustment zone were strongly influenced by the depression width.

Expanding the bed depression redistributed incoming flow laterally, increased energy losses through surface spreading, and shortened the effective forward reach of the dam-break wavefront due to enhanced dissipation (Fig. 13). Shifting the depression farther from the dam, from 1420 mm to 3490 mm, allowed the wave front to travel longer before encountering the bed depression. It also produced a fuller, more developed wave front at impact. When the bed depression was positioned farther downstream, the incoming flow exhibited a thicker, higher-energy front. It subsequently led to a more abrupt free-surface fall and a stronger splash zone. In contrast, depressions located closer to the dam intercepted the wave earlier, causing a shallower nappe and a more gradual flow transition into the downstream reach. The depression location also influenced where the hydraulic jump formed and how long it persisted. The downstream depression pushed the jump farther away from the dam, lengthening the energy dissipation region. Additionally, placing the depression at greater distances delayed the reflected disturbances from it, enabling a longer undisturbed propagation of the initial surge before significant energy loss occurred. Overall, the wave pattern and hydraulic adjustment zone were susceptible to depression location. Moving the bed depression downstream increased the impact intensity and splash generation (Fig. 14).

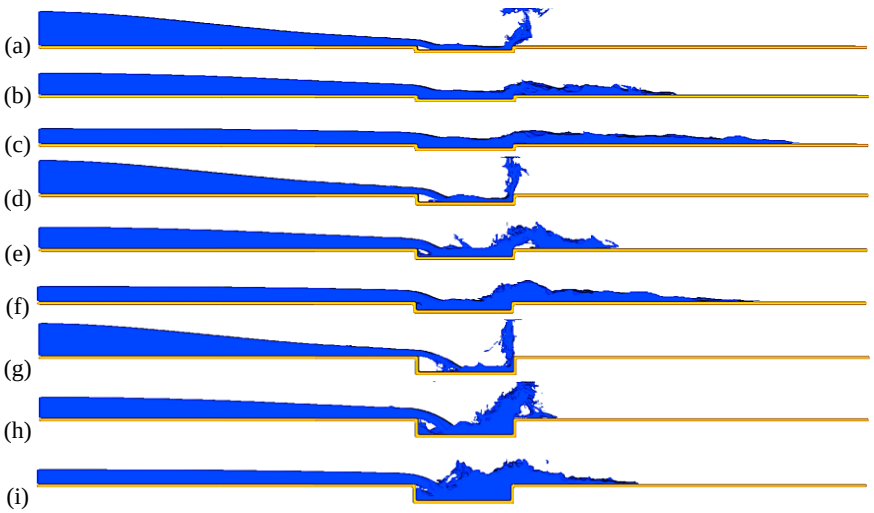

Fig. 11. Transient flow evolution over steps in different heights of (a) to (c) 27.5 mm, (d) to (f) 55 mm, and (g) to (i) 110 mm (up to down), at t = 1 s, 1.5 s, 2 s after starting the dam-break wave evolution.

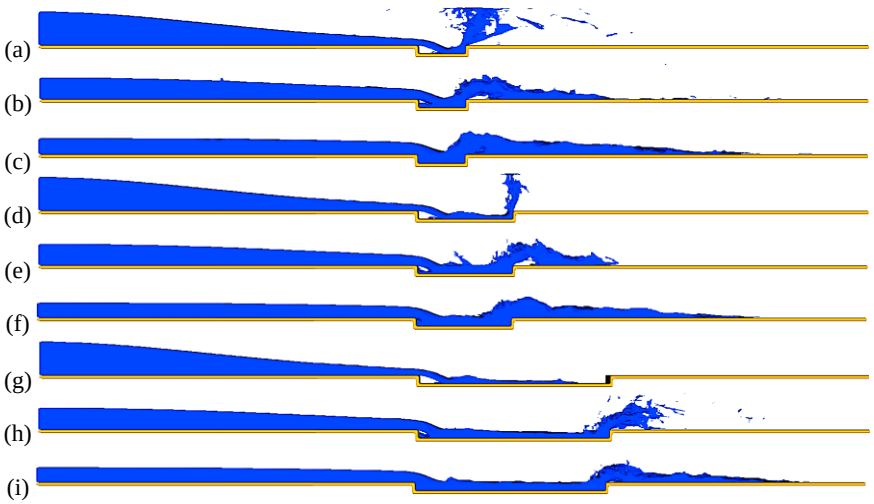

Fig. 12. Transient flow evolution over steps in different length of (a) to (c) 345 mm, (d) to (f) 690 mm, and (g) to (i) 1380 mm (up to down), at t = 1 s, 1.5 s, 2 s.

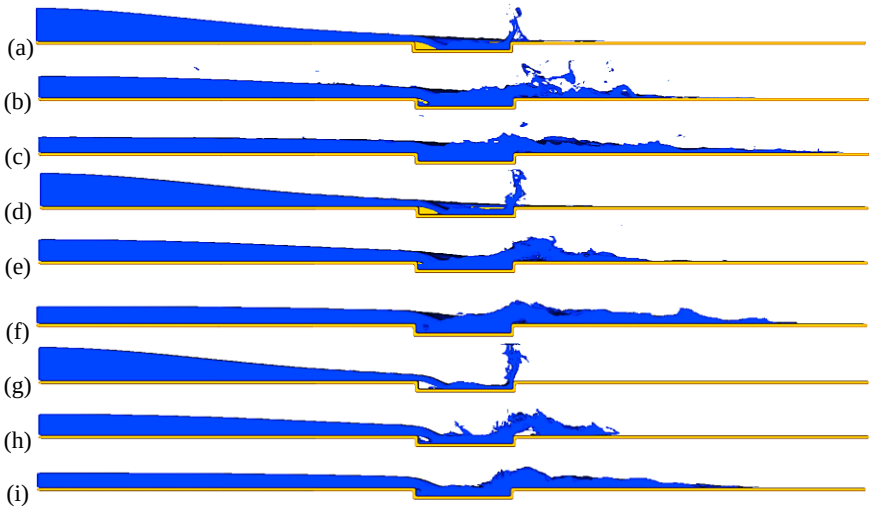

Fig. 13. Transient flow evolution over steps in different widths of (a) to (c) 50.5 mm, (d) to (f) 110 mm, and (g) to (i) 220 mm (up to down), at t = 1 s, 1.5 s, 2 s.

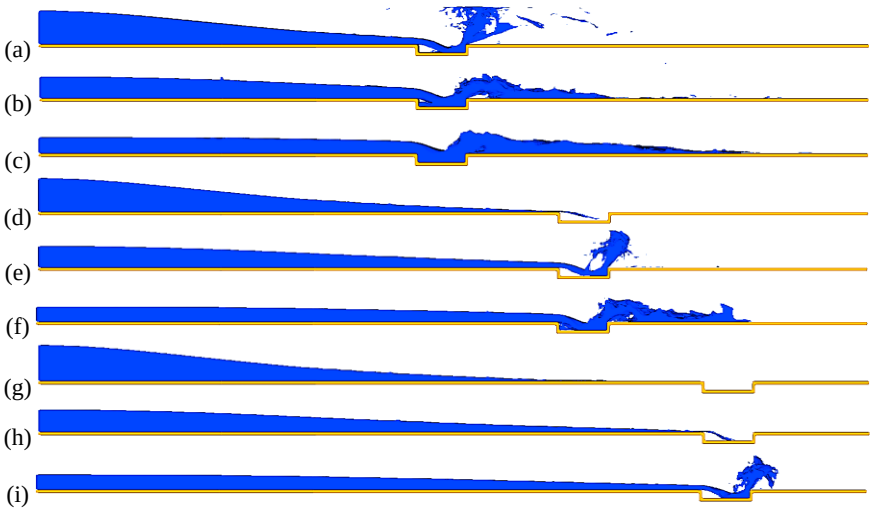

Fig. 14. Transient flow evolution over steps in different location of (a) to (c) 1420 mm, (d) to (f) 2455 mm, and (g) to (i) 3490 mm from the dam site, along the downstream channel at t = 1 s, 1.5 s, 2 s.

The three-dimensional simulations show that the early dam-break stage is governed by localized hydraulic transitions over the bed depression, which directly control energy dissipation, jet development, and the onset of peak loads. Within the first seconds after gate removal, the flow accelerates rapidly over the depression, producing strong vertical motions, near-bed separation, and transient supercritical conditions. These features

concentrate around the depression and dominate the near-field response during the initial impact phase.

To quantify these effects, the spatial distributions of flow depth (h) and Fr were extracted along the flume centerline during the early stage (t = 1–2 s), as presented in Figs. 15 and 16. The results clearly demonstrate that depression geometry strongly modifies the transient hydraulic structure.

The profiles in Fig. 15 further quantify how depression geometry modifies the near-field hydraulic response. Delineating the flow depth around the depression shows that increasing the depression height from shallow to deep raises the upstream depth immediately before the brink from approximately 0.10 m to 0.18 m at t = 1.5 **s** (Figs. 15a–c), resulting in a markedly steeper downstream free-surface fall. The deepest depression produces the most pronounced post-depression thinning, with a minimum depth close to 0.02 m, followed by gradual recovery to about 0.06 m within roughly 1.5 m downstream (Fig. 15c). In contrast, increasing the depression length reduces the pre-impact depth from around 0.15 m to 0.10 m and smooths the downstream descent (Figs. 15d–f), indicating a less abrupt hydraulic transition during the early transient stage. The extended geometry distributes the bed variation over a larger distance, weakening localized acceleration and reducing the severity of the near-field drawdown during the same early-time window. Consistent with these depth variations, Fr distributions (Fig. 16) show intensified supercritical regions over deeper depressions, while longer depressions reduce peak Fr values and shorten the spatial extent of extreme regimes. Overall, the results demonstrate that depression height amplifies hydraulic intensity, whereas depression length attenuates and smooths the transient response, with direct implications for early-stage flow regime transitions and associated impact dynamics.

In Fig. 15f (the longest depression), the nappe reattached gradually, and the downstream depth stabilized near 0.05–0.06 m without a strong rebound. In contrast, the shorter lengths induced a local hump around 1.2 m, reaching around 0.12 m, indicating stronger re-impact and localized energy release (Fig. 5d). Moreover, widening the bed depression spread the flow laterally and lowered the depth immediately after the brink (Figs. 15g-i). In Fig. 15g (the narrow depression), the depth peaked at around 0.18 m upstream and plunged to 0.03 m. In contrast, in the widest depression (Fig. 15i), the fall was gentler with a downstream depth plateau around 0.06 m and no sharp overshoot. The profiles of Figs. 15j to 15l (position change) showed that depressions farther downstream meet a more developed surge. The profile of Fig. 15l exhibited a tall pre-depression depth of about 0.22 m and an abrupt post- depression minimum of about 0.02 m, followed by slow recovery. However, there was a minor dip of ~0.05 m due to weaker flow energy in Fig. 15j. Overall, at the early stage (t = 1.5 s), depper depressions and downstream positions caused sharper depth steps immediately after the brink due to larger pre-depression depths and steeper free-surface gradients. However, the longer and wider depressions instead smoothed the initial free-surface fall, spreading energy laterally and reducing abrupt depth changes soon after impact.

3.3.1 Flow regime around the bed depression

Delineating Fr around the depression showed that increasing the depression height from shallow to deep (27.5 mm to 110 mm) raised the downstream velocity and produced a stronger supercritical zone just after the brink at t = 1.5 s (Figs. 16a–c). In the deepest depression, Fr climbed rapidly from subcritical upstream to about 5 just after the depression and remained supercritical over a longer reach (Fig. 16c). However, lengthening the depression, from 345 mm to 1380 mm, reduced the supercritical peak and extended a near-critical transition, indicating smoother acceleration and weaker jump formation (Figs. 16d–f). The shortest length in Fig. 16d produced a sharp supercritical spike of about 6 and an immediate localized hydraulic adjustment. In the longest depression, the flow was critical ($Fr \approx 1$) for most of the reattachment zone before rising only moderately to about 4–5 downstream (Fig. 16f).

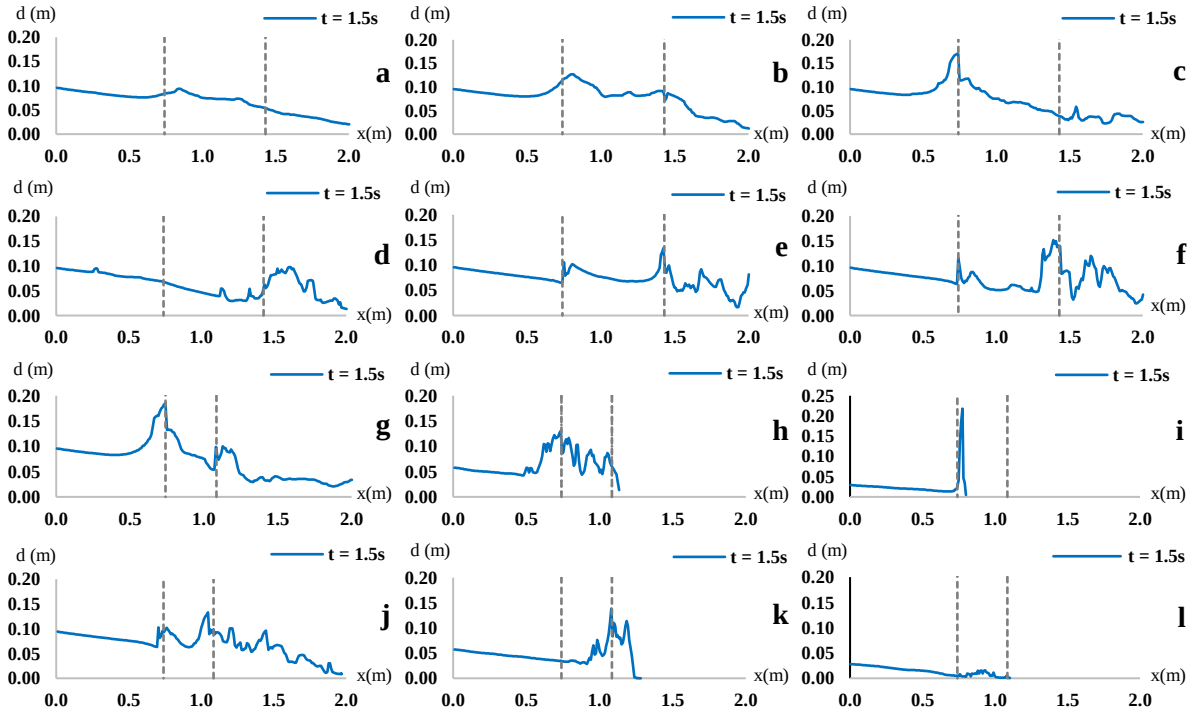

Fig. 15. Spatial variation of flow depth in central axes of flume and near steps with different (a) to (c) heights, (d) to (f) lengths, (g) to (i) widths, and (j) to (l) locations at t = 1 s, 1.5 s, and 2 s.

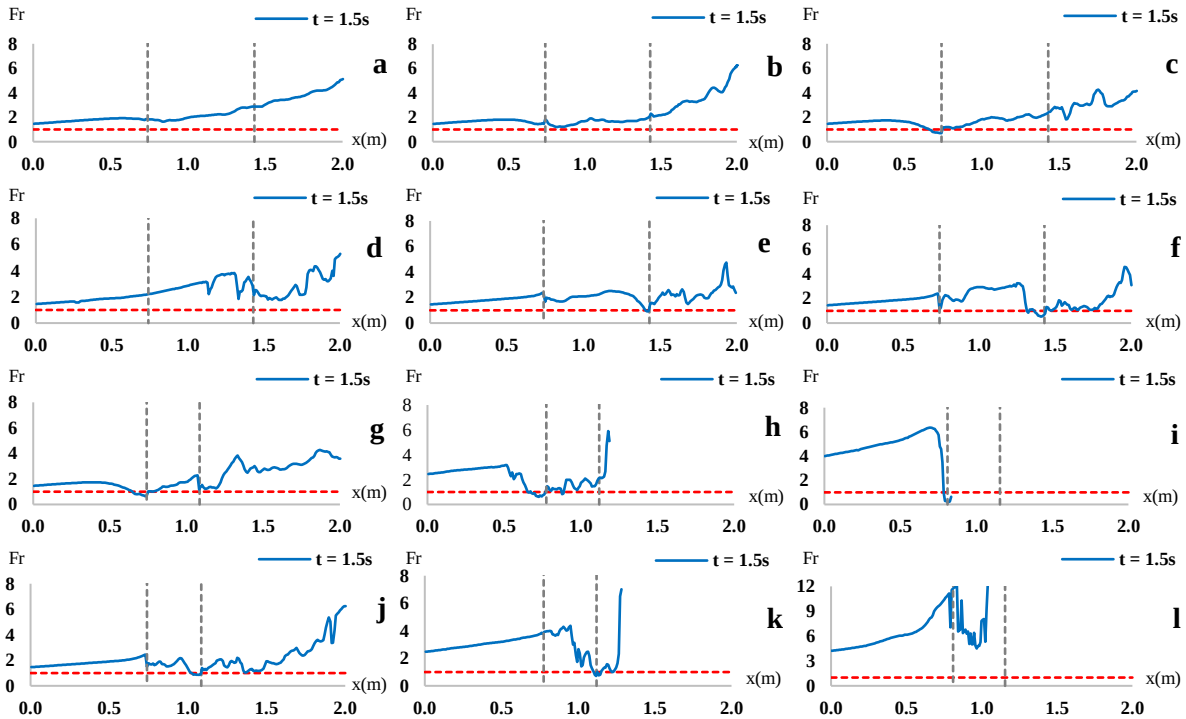

Fig. 16. Spatial variation of Fr in central axes of flume and near steps under the effect of the step's (a) to (c) height and depth, (d) to (f) length, (g) to (i) width, and (j) to (l) location.

Table 4. Summary of the effects of bed depression geometry and location on early-stage transient flow behavior and impact loading.

Geometric parameter	Increase in parameter leads to	Free-surface evolution	Flow regime (Fr)	Impact load variation
Depression height (H_d)	Deeper plunge pool and thicker nappe	Stronger surface breakup, delayed recovery	Extended supercritical reach ($Fr \approx 4$–12)	Higher peak force, longer force duration
Depression length (L_d)	Longer falling water sheet	Smoother downstream surface, delayed wave front	Reduced Fr peak, extended near-critical zone	Lower peak force, smoother decay
Depression width (W_d)	Enhanced lateral spreading	Thinner downstream depth, wider nappe	Suppressed Fr peak, faster stabilization	Reduced peak force via momentum redistribution
Depression location (L_1)	More developed surge at impact	Abrupt free-surface fall, stronger splash	Higher Fr peak downstream	Larger initial force peak

Moreover, widening the depression spread the discharge laterally and suppressed the Froude peak just past the brink (Figs. 16g–i). In Fig. 16g (the narrow depression), *Fr* increased abruptly to about 4–4.5, while in the widest depression (Fig. 16i), the flow stepped to near-critical and stayed subcritical farther downstream. The profiles of Figs. 16j–l (position change) showed that depressions placed farther downstream encounter a more developed surge. The profile of Fig. 16 (l) exhibited the largest supercritical peak, rising beyond *Fr* = 9–12, while the nearer depression in Fig. 16j peaked only around 5–6.

Overall, at the early stage, higher depression and downstream positions produced stronger and longer supercritical reaches, intensifying potential hydraulic jumps. However, longer and wider depressions reduced peak Fr, promoted near-critical transition, and smoothed the initial acceleration after the brink. Accordingly, Table 4 consolidates these trends by summarizing the early-stage hydraulic response across all. Simulated configurations, particularly, highlighting the distinct roles of depression height, length, width and downstream location. Specifically, increasing depression height and placing the depression farther downstream consistently intensified the supercritical regime, as reflected by higher peak Fr number and longer adjustment lengths. By contrast, increasing depression length and width attenuated the supercritical peak during the early stage. As a result, promoted an extended near-critical transition and moderated the acceleration of flow after the brink. Overall, by synthesizing the effects of individual geometric parameters, Table 4 provides a quantitative overview. Ultimately, bed depression geometry governs transient flow regime development during the initial surge phase.

These results confirmed several reported patterns but introduced clear advances. As noted by Cozzolino et al. (2018), depression changes reduce the wave celerity in transient flow evolution. However, in this study, deeper depressions created

extended supercritical reaches with Fr = 4–12 and sharp post-depressions (about 0.02 m). Furthermore, earlier laboratory studies by Ferrari et al. (2010) and Kocaman and Ozmen-Cagatay (2012) qualitatively described nappe breakup. Whereas the LES-based analysis of this study linked thicker nappes in deep depressions to sustained supercritical flow and delayed hydraulic-jump stabilization. Moreover, analytical studies, such as those by Deng et al. (2018), predicted wave tip behavior but lacked three-dimensional Froude mapping. In contrast, the results of this study showed that long, wide depressions suppress peaks at Fr = 2–3 and accelerate the return to near-critical flow. Previous energy-loss analyses by Lakzian and Estiri (2018), suggested that extended depressions dissipate energy. However, the current study quantified the resulting reduction in wave celerity and early hydraulic-jump strength using mesh-converged, turbulence-calibrated CFD. In addition, the field observations after dam removal by Harrison et al. (2018) documented delayed fronts but not near-depression regime shifts. In contrast, this work resolved early supercritical cores and hydraulic-jump migration with high-resolution three-dimensional modeling.

3.3.2 Impact load on the bed depression

Calculating the impact load from a dam-break wave on downstream structures is critical in assessing the potential damage from such events. Evaluating the impact force helps design structures, such as bridges and buildings, to withstand potential dam-failure floods and to develop emergency action plans (Aureli et al., 2015; Yang et al., 2023). This study estimated the temporal variation of impact load, the horizontal impact force, across the entire depression volume.

Increasing the depression height from shallow to deep significantly increased the initial force peak and delayed its decay at the early stage ($t \leq 3s$) (Fig. 17a). The deepest depression ($H_d = -0.11$) produced the most significant peak load of about 42 N within the first second and maintained forces above 10 N for nearly 3 s. However, the shallowest depression (H_d = –0.0275 m) peaked at less than 20 N and declined rapidly. However, lengthening the depression reduced the maximum impact considerably (Fig. 17b). The shortest depression (L_d = 0.345 m) generated a peak near 18 N, whereas the longest (L_d = 1.38 m) stayed below 10 N and showed a smoother decay, indicating progressive dissipation along the extended nappe. Moreover, widening the depression decreased the force intensity by spreading momentum laterally (Fig. 17c). The narrowest width (W_d = 0.0505 m) reached approximately 17 N, while the widest (W_d = 0.202 m) remained near 8-10 N and decayed quickly. The profiles of Fig. 17d (position change) showed that depressions farther downstream experienced higher initial loads due to the more developed surge. The farthest location (L_1 = 3.49 *m*) recorded an early spike around 24 N, compared with only around 10 N at the nearest location (L_1 = 1.42 m). Overall, deeper and downstream depressions intensified impact peaks and sustained forces longer, while greater length and width effectively reduced the maximum Fx and accelerated load dissipation. It is noted that the absolute impact forces reported in Fig. 17 correspond to laboratory-scale conditions. Under Froude similarity, prototype-scale impact loads scale with the cube of the geometric scale ratio, so that relatively small laboratory forces may correspond to substantially larger prototype forces (Ahmadi et al., 2025). Accordingly, the emphasis of the present analysis is on the relative amplification or attenuation of impact loads due to bed-depression geometry, which remains physically meaningful and transferable across scales.

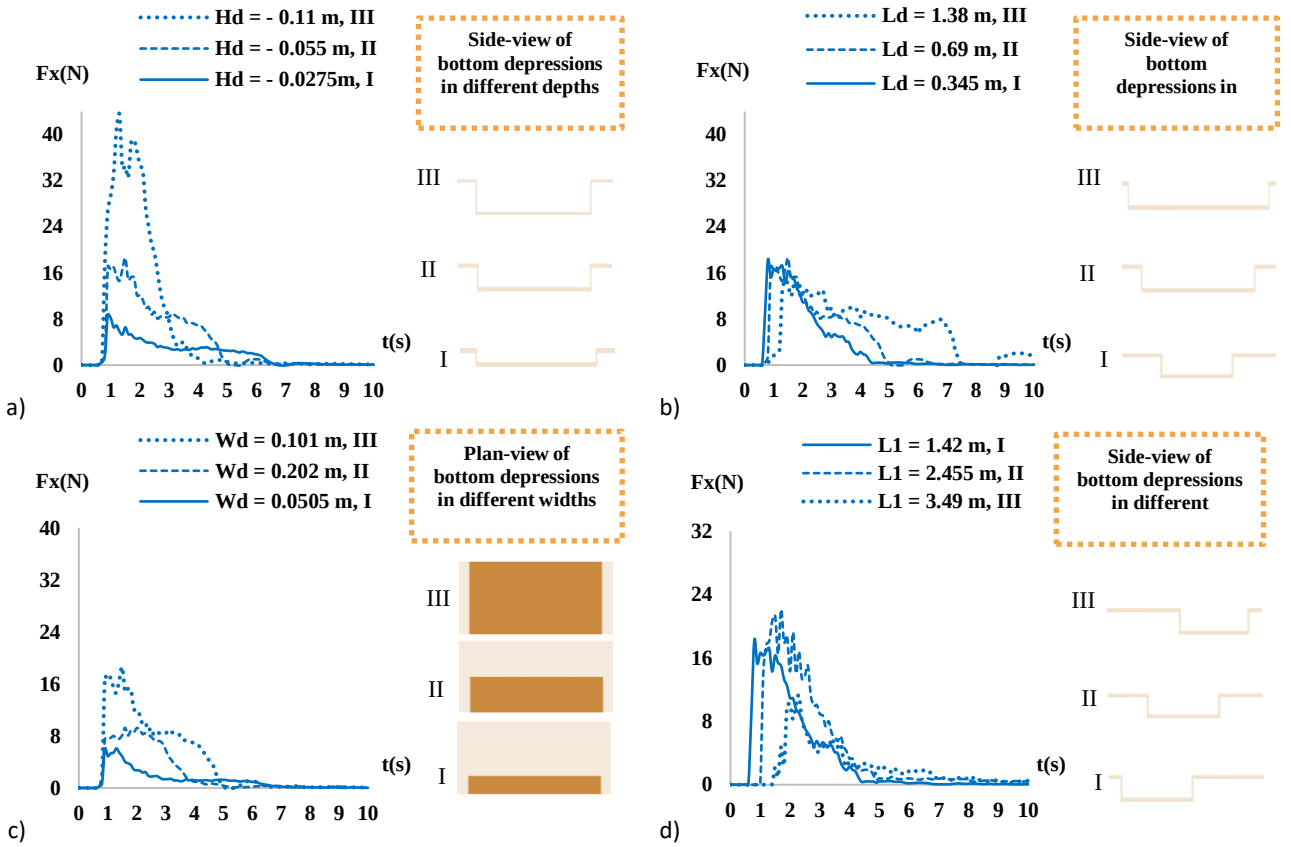

Fig. 17. The flow impact load over steps under the effect of the step's (a) height, (b) length, (c) width, and (d) location.

Despite these advances, some substantive limitations remain that qualify our conclusions, constrain generalizability, and motivate targeted avenues for future investigation. First, the bed and walls were fixed, excluding sediment transport, roughness heterogeneity, and scour-flow feedbacks. Second, air-water interfaces were resolved with a single-grid VOF, air entrainment module and one LES-SGS closure, under-resolving entrainment, spray breakup, and model-form uncertainty. Third, validation spanned few laboratory geometries and scales, so prototype Reynolds-Froude similarity and early-force bias were not fully assessed. Fourth, the classical hydromechanics provides analytical descriptions for steady, depth-averaged supercritical flows over idealized bed geometries (Bollrich, 2019). Such formulations allow the estimation of water levels and specific energy under quasi-one-dimensional assumptions. However, these approaches neglect strong transient effects, lateral spreading and three-dimensional flow structures that dominate dam-break-driven impacts. The present study, therefore, does not attempt a direct analytical prediction of water levels using steady hydromechanical theory. Instead, classical formulations are regarded as limiting reference solutions, whereas the numerical and experimental results address transient supercritical regimes beyond the validity of steady assumptions.

The results presented herein provide quantitative performance metrics in terms of flow regime development and impact load evolution across a controlled set of geometric configurations. The emphasis is placed on identifying dominant trends and relative sensitivities rather than deriving explicit empirical or nondimensional design relationships. While such correlations are valuable for direct engineering application, their development requires a broader parameter space and additional scale-bridging validation beyond the scope of the present study. Accordingly, the reported results are intended to serve as a physically consistent basis for comparative assessment and future formulation of practical design tools.

For future studies it is suggested that 3D-CFD be coupled with mobile-bed morphodynamics and fluid-structure interaction, with calibrated roughness and instrumented scour to capture two-way feedbacks. Furthermore, it is suggested that dynamic SGS closures (e.g., WALE, dynamic Smagorinsky), adaptive meshing, and interface-sharpening be employed, alongside time-resolved PIV/pressure for near-field validation. In addition, the geometry-scale matrix should be extended to prototype conditions, integrating GIS-CFD-ML surrogates to derive design thresholds for Fr peaks, jump location and impact loads.

4 CONCLUSIONS

Dam-break floods arise from sudden barrier failure, releasing water that generates rapidly varying, highly transient flows. These transient flows are characterized by rapid changes in depth, velocity, and free surface that govern energy release, impact loading, and hydraulic-jumps developments during the flood evolution. However, bed singularities from topography or in-channel infrastructures redirect momentum and shift flood regime transitions, amplifying supercritical zones, hydraulic jumps and scour risk. This study investigated the transient dam-break flow hydrodynamics over a bed depression in a prismatic channel. The study employed mesh-verified, LES-calibrated 3D-VOF modeling with laboratory validation using the dam-break data existing in literature. The model was then used to predict the free surface evolution, Froude regime, and time-resolved impact forces for various bed-depression height, length, width and downstream location. The critical results of this study were as follows:

- The agreement between modeling and experimental results was strong for transient flow depth with R^2 about 0.99, and RMSE between 0.006 m – 0.007 m and for velocity with RMSE about 0.065 m/s.
- Transient flow depths showed sharp drawdown across the bed depression with localized backflow**.** Increasing depression height raised the upstream maximum depth from 0.09 m to 0.23 m, while post-depression minima reached to about 0.02 m.
- Deeper and farther-downstream depressions produced extended supercritical reaches ($Fr \approx 4–12$), sharp post-depression minima (about 0.02 *m*), and larger, longer-lasting forces (about 24 N–42 N).
- Longer and wider depressions suppressed peak Froude number to about 2–3, stabilized downstream depths about 0.05–0.06 m, and limited impact load levels to about 8–10 N.

These findings establish geometry-based thresholds linking bed-depression configuration to early energy release, hydraulic-jump stabilization, and near-field loading. These thresholds enable risk-based sizing and placement of engineered bed-depression, improving flood routing, public safety, and cost-effective scour protection and maintenance.

Acknowledgement: The authors would appreciate the collaboration of all colleagues and scholars with constructive feedback on different aspects of this work.

REFERENCES

Abdedou, A., Soulaïmani, A., Tchamen, G.W., 2020. Uncertainty propagation of dam-break flow using the stochastic non-intrusive B-splines Bézier elements-based method. Journal of Hydrology, 590, 125342.

Ahmadi, R., Afzalimehr, H., Abed, H.J., Okhravi, S., 2025. Hydrodynamic effects of porous baskets on scour patterns at elliptical and hexagonal piers. Journal of Hydrology and Hydromechanics, 73(3), 230-247.

Albu, L.M., Enea, A., Iosub, M., Breabăn, I.G., 2020. Dam breach size comparison for flood simulations. A HEC-RAS based, GIS approach for Drăcșani Lake, Sitna River, Romania. Water, 12(4), 1090.

Aureli, F., Dazzi, S., Maranzoni, A., Mignosa, P., Vacondio, R., 2015. Experimental and numerical evaluation of the force due to the impact of a dam-break wave on a structure. Advances in Water Resources, 76, 29-42.

Aureli, F., Maranzoni, A., Petaccia, G., Soares-Frazão, S., 2023. Review of experimental investigations of dam-break flows over fixed bottom. Water, 15(6), 1229.

Bollrich, G., 2019. Technical hydromechanics 1: Fundamentals (8th rev. ed.). DIN Media Verlag (Original work published in German).

Catucci, D., Briganti, R., Heller, V., 2021. Numerical validation of novel scaling laws for air entrainment in water. Proceedings of the Royal Society A: Mathematical, Physical and Engineering Sciences, 477(2255).

Cozzolino, L., Pepe, V., Cimorelli, L., D'Aniello, A., Della Morte, R., Pianese, D., 2018. The solution of the dam-break

problem in the porous shallow water equations. Advances in water resources, 114, 83-101.

Deng, X., Liu, H., Lu, S., 2018. Analytical study of dam-break wave tip region. Journal of Hydraulic Engineering, 144(5), 04018015.

Dezert, T., Kiplesund, G.H., Sigtryggsdóttir, F.G., 2024. Parametric breach model evaluation from laboratory rockfill dam models under overtopping conditions. Journal of Hydraulic Engineering, 150(6), 04024046.

Fan, J. H., Galoie, M., Motamedi, A., 2020. Mitigation of the amplitude and celerity of dam-break shock wave using combination of groyne and vertical pier. Journal of Mountain Science, 17(6), 1452-1461.

Fan, J., Motamedi, A., Galoie, M., 2021. Impact of downstream lakes on dam-break wave attenuation. Natural hazards, 106(1), 595-612.

Ferrari, A., Fraccarollo, L., Dumbser, M., Toro, E.F., Armanini, A., 2010. Three-dimensional flow evolution after a dam-break. Journal of Fluid Mechanics, 663, 456-477.

FLOW-3D® Version 13, 2020. Santa Fe, NM: Flow Science, Inc. https://flow3d.com

Harrison, L.R., East, A.E., Smith, D.P., Logan, J.B., Bond, R.M., Nicol, C. L., Williams, H.T., Boughton, A.D., Chow, K., Luna, L., 2018. River response to large-dam removal in a Mediterranean hydroclimatic setting: Carmel River, California, USA. Earth Surface Processes and Landforms, 43(15), 3009-3021.

Heidarian, P., Neyshabouri, S.A.A.S., Khoshkonesh, A., Nazari, R., Okhravi, S., Di Francesco, S., 2025. Numerical study of downstream sediment scouring of the slotted roller bucket system. Water, 17(16), 2471.

Heller, V., 2011. Scale effects in physical hydraulic engineering models. Journal of Hydraulic Research, 49(3), 293-306.

Hien, L.T.T., Van Chien, N., 2021. Investigate impact force of dam-break flow against structures by both 2d and 3d numerical simulations. Water, 13(3), 344.

Hirt, C.W., Nichols, B.D., 1981. Volume of fluid (VOF) method for the dynamics of free boundaries. Journal of Computational Physics, 39(1), 201–225.

Hui, X., Fu, X., Peng, M., Zhang, G., Shi, Z., Zhu, Y., 2024. Experimental and numerical study on the breaching mechanisms of landslide dams with non-uniform structures. Engineering Geology, 330, 107414.

Khoshkonesh, A., Nsom, B., Gohari, S., Banejad, H., 2019. A comprehensive study on dam-break flow over dry and wet beds. Ocean Engineering, 188, 106279.

Khoshkonesh, A., Nsom, B., Okhravi, S., Dehrashid, F.A., Heidarian, P., DiFrancesco, S., 2024. Numerical investigation of dam-break flow over erodible beds with diverse substrate level variations. Journal of Hydrology and Hydromechanics, 72(1), 80-94.

Kleefsman, K.M.T., Fekken, G., Veldman, A.E.P., Iwanowski, B., Buchner, B., 2005. A volume-of-fluid based simulation method for wave impact problems. Journal of computational physics, 206(1), 363-393.

Kocaman, S., Evangelista, S., Guzel, H., Dal, K., Yilmaz, A., Viccione, G., 2021. Experimental and numerical investigation of 3d dam-break wave propagation in an enclosed domain with dry and wet bottom. Applied Sciences, 11(12), 5638.

Kocaman, S., Ozmen-Cagatay, H., 2012. The effect of lateral channel contraction on dam-break flows: Laboratory experiment. Journal of hydrology, 432, 145-153.

Koshizuka, S., Y. Oka., 1996. Moving-particle semi-implicit method for fragmentation of incompressible Fluid. Nuclear Science and Engineering 123: 421-434. doi:10.13182/NSE96-A24205.

Lakzian, E., Estiri, A., 2018. Entropy generation analysis as design criteria in dam-break flows for non-Newtonian fluids. The European Physical Journal Plus, 133(11), 454.

Liu, K., Zhang, J., He, X., Peng, H., 2025. Spatiotemporal dam-break flood impact loads: Experimental study and deep learning analysis. Ocean Engineering, 319, 120200.

Ma, J., Xu, C., Chen, J., 2025. Dam-breach process simulation and risk assessment of outburst flood induced by the Tangjiashan landslide-dammed lake. Journal of Hydrology: Regional Studies, 57, 102164.

Mahmoud, A.A., Uchida, T., 2024. Dam-break flow through rigid-emergent vegetation. Experiments in Fluids, 65(11), 169.

Maranzoni, A., D'Oria, M., Rizzo, C., 2024. Probabilistic mapping of life loss due to dam-break flooding. Natural Hazards, 120(3), 2433-2460.

Maskoni, A., Latrache, N., Khoshkonesh, A., Asim, T., Polidori, G., Mishra, R., Nsom, B., 2023. Stability of viscous lubricated thin film down an inclined plane beneath ambient lighter non-miscible static liquid. International Journal of COMADEM, 26(1), 5–12.

Mattas, C., Karpouzos, D., Georgiou, P., Tsapanos, T., 2023. Two-dimensional modeling for dam-break analysis and flood hazard mapping: a case study of Papadia Dam, Northern Greece. Water, 15(5), 994.

Meng, W., Yu, C. H., Li, J., An, R., 2022. Three-dimensional simulation of silted-up dam-break flow striking a rigid structure. Ocean Engineering, 261, 112042.

Ni, Y., Cao, Z., Liu, Q., 2019. Mathematical modeling of shallow-water flows on steep slopes. Journal of Hydrology and Hydromechanics, 67(3), 252-259.

Oguzhan, S., Aksoy, A.O., 2020. Experimental investigation of the effect of vegetation on dam-break flood waves. Journal of Hydrology and Hydromechanics, 68(3), 231-241.

Okhravi, S., Gohari, S., Alemi, M., Maia, R., 2023. Numerical modeling of local scour of non-uniform graded sediment for two arrangements of pile groups. International Journal of Sediment Research, 38(4), 597-614.

Oyem, E.U., Khoshkonesh, A., Nsom, B., 2025. Numerical study of wind-driven natural ventilation in Lagos. In 2025 International Conference on Emerging Technologies and Computing (IC_ETC) (pp. 1–5). IEEE.

Pandey, B. R., Knoblauch, H., Zenz, G., 2024. Potential dam breach flood assessment with the 2D diffusion and full dynamic wave equations using a Hydrologic Engineering Center-River Analysis System. Water, 16(2), 277.

Rahimpour, A., Afzalimehr, H., Okhravi, S., Nazari-Sharabian, M., Karakouzian, M., 2026. Turbulence in a bend in the presence of emergent vegetation and a 3D pool bedform. Water, 18(3), 431.

Rajaie, M., Azimi, A.H., Nistor, I., Rennie, C.D., 2022. Experimental investigations on hydrodynamic characteristics of tsunami-like hydraulic bores impacting a square structure. Journal of Hydraulic Engineering, 148(3), 04021061.

Říha, J., Duchan, D., Zachoval, Z., Erpicum, S., Archambeau, P., Pirotton, M., Dewals, B., 2019. Performance of a shallow-water model for simulating flow over trapezoidal broad-crested weirs. Journal of Hydrology and Hydromechanics., 67 (4), 322 - 328.

Velísková, Y., Chára, Z., Schügerl, R., Dulovičová, R., 2018. CFD simulation of flow behind overflooded obstacle.

Journal of Hydrology and Hydromechanics, 66 (4), 448 - 456.

Wang, B., Liu, X., Zhang, J., Guo, Y., Chen, Y., Peng, Y., Liu, W., Yang, S., Zhang, F., 2020. Analytical and experimental investigations of dam-break flows in triangular channels with wet-bed conditions. Journal of Hydraulic Engineering, 146(10), 04020070.

Xu, J., Zhang, Y., Ma, Q., Zhang, J., Hu, Q., Zhan, Y., 2025. Dam-break hazard assessment with CFD computational fluid dynamics modeling: The Tianchi Dam Case Study. Water, 17(1), 108.

Yang, M., Cai, Q., Li, Z., Yang, J. 2023. Uncertainty analysis on flood routing of embankment dam breach due to overtopping failure. Scientific Reports, 13(1), 20151.

Zhou, G.G., Lu, X., Xie, Y., Cui, K.F., Tang, H., 2022. Mechanisms of the Non-Uniform breach morphology evolution of landslide dams composed of unconsolidated sediments during overtopping failure. Journal of Geophysical Research: Earth Surface, 127(10), e2022JF006664.

Zhu, Y., Hu, D., 2018. Vertical 2D nonhydrostatic model using mode splitting for dam-break flows. Journal of Hydraulic Engineering, 144(6), 06018008.

Received 29 October 2025
Accepted 3 March 2026